Journal of Magnetism and Magnetic Materials 622 (2025) 172959

Contents lists available at ScienceDirect

Journal of Magnetism and Magnetic Materials

journal homepage: www.elsevier.com/locate/jmmm

Research article

A sinusoidal magnetization distribution as an original way to generate a versatile magnonic crystal for magnon propagation

P. Micaletti [a], A. Roxburgh [b], E. Iacocca [b], M. Marzolla [c], F. Montoncello [a,*]

[a] Dipartimento di Fisica e Scienze della Terra, Università di Ferrara, via G. Saragat, 1, Ferrara, 44122, Italy
[b] Department of Physics and Energy Science, University of Colorado at Colorado Springs, 1420 Austin Bluffs Parkway, Colorado Springs, 80918, CO, USA
[c] Dipartimento di Informatica–Scienza e Ingegneria, Università di Bologna, Mura Anteo Zamboni, 7, Bologna, 40126, Italy

ARTICLE INFO

Keywords:
Spin waves
Magnonic crystals
Band diagram
Micromagnetism

ABSTRACT

The manipulation of the magnetization in a film at the nanoscale is one of the best means for controlling spin-wave propagation in real time. In 3D Magnonics, the vertical or interfacial interaction with patterned layers can make the film magnetization depart from uniformity, which, in general, can introduce new spin-wave modes in the film, hence additional degrees of freedom for signal manipulation. In this paper, we suggest a sinusoidal distribution for the magnetization as an original and effective way to generate a magnonic crystal and control its magnon dynamics. Along with a uniform bias field, we introduce in the film layer a sinusoidal bias field, simulating the vertical/interfacial interaction with other layers: after relaxation, the film magnetization assumes a sinusoidal equilibrium distribution. Using micromagnetic simulations followed by Fourier analysis, we show how to control the magnon dynamics by tuning the magnetization undulation amplitude and symmetry. We compute the magnon dispersion curves and space profiles, we show the occurrence of new degrees of freedom for signal manipulation and the rise of localized and stationary magnon modes. We highlight the physical mechanisms governing the occurrence and variation of the frequency-gap at zone-boundary. Finally, we indicate how to practically implement a sinusoidal field (and consequent magnetization) when the vertical coupling is the inverse magnetoelastic interaction between ferroelectric and ferromagnetic films. Our results suggest a new mechanism for controlling magnon propagation, which appears extremely appealing for its really wide range of tunable effects on their dynamics, particularly interesting in the engineering of signal filtering, information storage and delivery, and sensing activity.

1. Introduction

One of the biggest challenges in modern research is the conception of portable, multifunctional, environmentally friendly devices [1,2]. Miniaturization is certainly a key factor, however for the past two decades it has been clear that there is a limit below which the benefit of miniaturization is lost by the overheating of chips at the nanoscale (due to electron scattering), failing in efficiency and portability [3]. This explains in particular why current processor clock rates are almost the same as 20 years ago [2]. Furthermore, growing concerns regarding the carbon footprint of everyday devices demonstrate the urgency for alternatives to ordinary electronics [4].

A possible solution is to attain data transfer and manipulation by spin waves (SWs), which do not involve any charge motion, thereby producing minimal waste heat [5–7]. Moreover, at the GHz regime SWs have nanometric wavelengths, and hence are suitable for miniaturization purposes. In particular, it is possible to influence the SW propagation properties through Bragg diffraction after designing appropriate geometries in the ferromagnetic medium within which SWs are confined [8–18]. More recently, due to improved fabrication techniques, the exploration of SW physics in three-dimensional (3D) periodic arrangements or stacks of layers with different geometries [19–22] has unveiled new possibilities such as reconfigurable spin-wave microstate fingerprinting [23–25] and interlayer dynamic coupling [26–29], which are particularly promising in the perspective of controlling magnons at the nanoscale. The Dzyaloshinskii–Moriya interaction (DMI), forming at the interface with metal layers, can be thought of as a vertical (interfacial) interaction as well [9,30,31]. This interfacial interaction is extremely appealing, e.g., since it can provide the system dynamics with a magnonic frequency comb for signal multiplexing [32], and non-reciprocal dispersions and magnonic mode localization [33]. Furthermore, its dependence on the electric fields

* Corresponding author.
E-mail address: montoncello@fe.infn.it (F. Montoncello).

https://doi.org/10.1016/j.jmmm.2025.172959
Received 30 November 2024; Received in revised form 4 March 2025; Accepted 11 March 2025
Available online 22 March 2025

allows a strain-mediated magnetoelectric coupling between layers [34], which is promising for voltage-driven SW dynamics.

Most interestingly, in recent years many studies showed the possibility of creating a temperature-activated magnonic crystal in the film layer of a ferromagnet/superconductor hybrid metamaterial (e.g., Nb/Permalloy/Nb trilayer), thanks to the stray fields (vertical coupling) generated by the periodic superconducting structures when entering the Meissner (diamagnetic) state at temperature $T < T_c \equiv 9\ K$. The induced periodicity was confirmed by experimental verification of the occurring band gaps at zone boundary [35–38].

In summary, in a magnonic 3D structure, the top layer would act as a gate to control periodicity, group velocity, and phase of spin waves. Among the many possible 3D structures, an attractive category is composed of a ferromagnetic waveguide capped with a different layer to imprint on and modify the spin wave properties by vertical coupling [33,39]. In this context, the calculation of the SW dispersion in a film with a non-uniform magnetization, due to the vertical interaction, is indeed a crucial issue: depending on the group velocity at a given wavevector, and on the allowed and forbidden band widths, it is possible to design new devices with enhanced functionalities.

Our work has precisely that purpose: we present the sinusoidal distribution of the magnetization as an original way to generate a magnonic crystal, showing how its symmetry and amplitude can control the typical features in the magnon dynamics, like dispersion slope and curvature, allowed and forbidden bandwidths, localized and stationary modes. We consider a film with a sinusoidal magnetization (Fig. 1) determined by a likewise sinusoidal bias field[40], which can be thought of as the simulation of a vertical (or interfacial) interaction resulting from the film being part of a 3D system with appropriate geometry. We show the simulated dispersion relations $f(k)$ (i.e., frequency vs. wavevector) as a function of the sinusoidal field magnitude B_S, and discuss the appearance of frequency gaps and stationary solutions as the undulation amplitude of the magnetization increases. Note how, in the sinusoidal field B_S of Fig. 2(a), the fan angle (i.e., the angular spread of the vector field) is fixed to $\theta_F = \pi/2$. The corresponding relaxed magnetization [Fig. 2(b)] shows instead a reduced fan angle, due to the constant presence of the uniform bias field B_0, in addition to B_S. We also consider magnetization distributions following the relaxation to a chiral field, namely a vector field with a fan angle $\theta_F = 2\pi$, covering the full angle along a period [Fig. 2(c)]. This affects the symmetry of the corresponding relaxed magnetization, but not the sign of its x-component: hence the resulting magnetization is always sinusoidal, though asymmetric [Fig. 2(d)]. We will show how this case produces a richer dispersion diagram with localized, stationary modes that are strongly sensitive, in number and frequency, to the variation of the sinusoidal field magnitude. The simultaneous presence of localized and propagating modes at a few MHz of frequency separation, and with a similar profile symmetry, is particularly attractive in the context of signal processing in magnonics and spin-wave computing [5,6,41].

A sinusoidal distribution of the static magnetization in thin films was first observed by electron microscopy in 1960 by Fuller and Hale [42]. Many attempts were made soon after to provide the theoretical description of such a natural effect, along with hypotheses around its physical origin, e.g., surface roughness, magnetic anisotropy due to inverse magnetostriction, etc.[43–45]. In our work, not only do we deal with shorter undulation wavelengths (close to the exchange-dominated limit), but also we focus on the effects induced on the spin-wave dynamics. In particular, we make a conceptual jump: we suggest to purposely create the magnetization undulation with a tunable amplitude to control magnons at the nanoscale. This is clearly a new concept, which brings along new physics.

Achieving a sinusoidal magnetization in a film can have practical applications, particularly in the context of 3D Magnonics [20,46,47].

In a stack of layers with different geometries or material properties, an appropriate distribution of macrospins or ferroelectric domains could create a periodic, non-uniform interaction field impressing in the film layer a corresponding sinusoidal, non-uniform magnetization. The control of the sinusoidal field amplitude, either by manipulation of the macrospin orientation in the ASI layer, or (as we suggest in Section 4) by a voltage-driven ferroelectric domains in multiferroic stacks, determines the corresponding magnetization amplitude, which in turn changes the magnonic band diagrams and the spin dynamics.

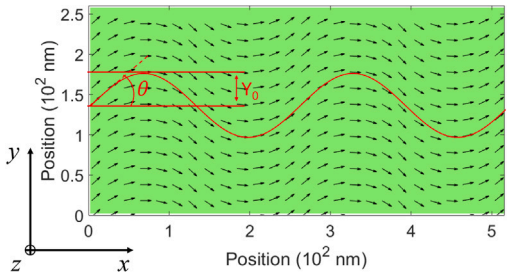

Fig. 1. Generic ground state with a sinusoidal magnetization and the reference system. The angle $\theta \equiv \theta_F/2$ is the slope of the magnetization at $x = 0$, while Y_0 is the spatial amplitude of the undulation, namely the maximum deflection from the ideal straight magnetization direction of an isolated film.

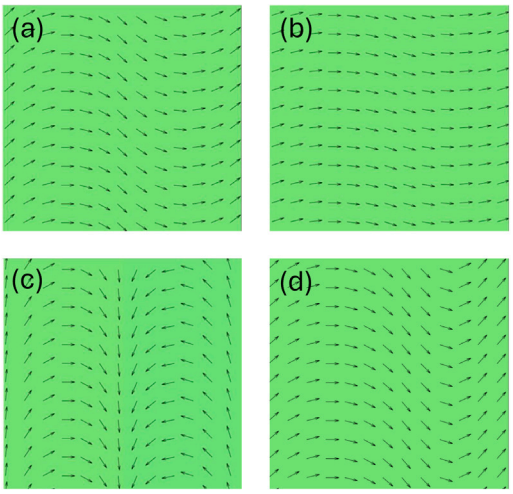

Fig. 2. Sketches of the vector field distributions subject of the investigation (the color marks the background, the arrows are only illustrative of the undulation). Panel (a): sine field which, combined with the uniform one, results, after relaxation, in the magnetization shown in panel (b). Panel (c): chiral field which, combined with the uniform one, results, after relaxation, in the magnetization shown in panel (d). In (d) the magnetization curvature is more pronounced in the second half of the primitive cell.

Our results shed light on the complexity of the dynamics in 3D magnonic architectures and directly address the engineering of signal filtering, information storage and delivery, and sensing activity. The ultimate purpose of our work is to show the potential of the magnon dynamics emerging from the undulation itself, in order to provide motivations and spurs for both the practical realization of such a magnetic configuration and the experimental/applicative investigation.

2. Methodology and ground states

Micromagnetic simulations are carried out by means of the graphic processing unit accelerated software MuMax3 [48]. We assume the magnetic parameters of permalloy, therefore: saturation magnetization $M_S = 800$ kA/m, exchange constant $A = 10$ pJ/m, and gyromagnetic ratio $\gamma = 185$ rad GHz/T. We consider a 5 nm-thick film with a periodic distribution of the magnetization, a lattice constant (period) $a = 256$ nm, and the primitive cell volume is $256\times256\times5$ nm^3. The geometric Brillouin zone (BZ) width is hence $\Delta k = 2\pi/a = 0.0245$ rad/nm, and in

the following we will address also a wider BZ, $\Delta k = 0.0490$ rad/nm, due to an additional magnetization symmetry.

Since our aim is to compute the dispersion curves by Fourier analysis, we replicate the volume 200 times along the x direction, so that the supercell is $51200\times256\times 5$ nm^3. The latter is discretized into $4\times4\times5$ nm^3 micromagnetic cells. As a consequence, each primitive cell consists of $64 \times 64 \times 1$ micromagnetic cells. With the magnetic parameters above, the exchange length, below which the spins are spontaneously aligned, turns out to be $\lambda_{ex} = 4.99$ nm. This observation justifies our choice of an elemental cell of 4 nm. We use quasi-periodic boundary conditions [49], namely 800 copies of the primitive cell along the x and y coordinates to mimic an extended, realistic thin film.

In our investigation, we take into account both in-plane and out-of-plane undulations, as well as dispersions with k parallel and perpendicular to the average magnetization direction (assumed along the x-axis), corresponding to backward volume spin waves (BA) and Damon–Eshbach surface spin waves (DE), respectively [50]. With reference to Fig. 1, to quantify the undulation amplitude Y_0, we consider the relative amplitude of the magnetization components $A = m_y^0/m_x^0$, taken at $x = 0$. Hence, Y_0 can be seen as the spatial deflection from the reference case of a uniform magnetization ($A = 0$). It can be shown how, holding the metric relationship:

$$y(x) = Y_0 \ \sin\frac{2\pi}{a}x \tag{1}$$

and considering the slope $\theta = \arctan(A)$, which is a half of the fan angle ($\theta_F = 2\theta$), we obtain the expression $Y_0 = A\frac{a}{2\pi}$. Even if in the following we will refer only to A, we find it helpful to mention here the concept of spatial extension for practical applications: it is very useful to correlate the ratio between the magnetization components and the actual spatial deflection of the undulation along y (i.e., the amplitude Y_0). For example, in our geometry, $A = 0.5$ implies an amplitude $Y_0 \approx 20.4$ nm. This piece of information is useful not only at the fabrication stage, to design the appropriate geometry and embrace all the desired amplitudes (e.g., if stripes, and not just films, were involved), but also at the characterization stage, when magnetic-force-microscopy or space-resolved Kerr magnetometry are concerned for the analysis of the real samples.

The plan of the investigation is the following. First, we isolate the effects in the SW dynamics due to the sole fact of having a sinusoidal periodicity of the film magnetization (Fig. 1), with a period equal to the length of the primitive cell. We consider different amplitudes ($A = m_y^0/m_x^0 = 0, 0.1, 0.2, 0.3...$). Such states, however, are not at equilibrium, particularly as we apply a uniform bias field $B_0 = 0.1$ T. Therefore, we perform conservative simulations (eliminating damping), which is unrealistic but artificially preserves the undulated magnetization in a (fictitious) stable equilibrium state. This allows us to compare the resulting dynamics with those of a uniformly magnetized film. We remark how, in keeping zero damping, our simulations indirectly assume that there is indeed a "physical cause" of such a non-uniform distribution, which we assume, at this stage of the investigation, to have no (or too little) influence on the spin-wave modes. For instance, an interaction (say, inverse-magnetostriction) could be strong enough to create a slight magnetization undulation, and hence induce the periodicity, but not so strong to lift the degeneracy of the stationary modes forming at zone boundary beyond the observation/measurement resolution. As we will see, this step in the strategy is necessary just to understand that the magnonic frequency gaps originate from the interaction of the SW modes with the "physical cause" of the magnetization curvature.

In a second and more realistic approach, we generate the sinusoidal magnetization as the relaxation of an initially uniform distribution to a sinusoidal bias field $B_S(x, y)$ [Fig. 2, panel (a)], which is added to the uniform bias field $B_0 = 0.1$ T. This method is particularly interesting because the sine-field keeps the undulated magnetization at equilibrium in the presence of a non vanishing damping. Moreover, the sine-field realistically mimics a possible vertical (or interfacial) interaction with some other layer which, due to its special geometry or material, can be responsible for such non-uniform distribution. Here, we expect to see the effects of the dynamic interaction with the physical cause of the non-uniform magnetization. After relaxation, the magnetization is at equilibrium in a sinusoidal distribution [Fig. 2, panel (b)]. We will address this case as a magnetization undulation polarized in the xy-plane. Note how B_S can be seen as a non-chiral vector field, in the sense that the rotation of the field vector is not complete (i.e., smaller than 2π) [Fig. 2(a)] [51]. Based on this observation, we consider a chiral vector field B_C in the third step, namely a field flux completing the 2π rotation along the x-axis [Fig. 2, panel (c)]. The resulting relaxed magnetization [Fig. 2, panel (d)] is always in a sinusoidal distribution (i.e., not chiral), however here the left–right symmetry of the primitive cell is broken, since magnetization and B_C point locally to either the same (panels (c-d), left half) or the opposite direction (panel (c-d), right half). Hence the magnetization undulation in the two halves of the primitive cell is no longer equivalent. Finally, we investigate the effects of an undulation polarized in the xz plane (i.e., out-of-plane undulation).

We observe that even when applying a chiral vector field, the resulting magnetization is not chiral (see for example Fig. 2(d)), nor is any of the involved interactions: careful inspection of the dispersion relations across $k = 0$ demonstrates that the results are reciprocal, regardless of the undulation polarization or wavevector direction[52].

In order to calculate, by Fourier analysis, the dispersion curves and the SW space profiles [53], we apply a sinc microwave field for a total time of 100 ns, defining the frequency resolution to $\delta f = 0.01$ GHz. We record the time-resolved spatial maps at a time interval $\delta t = 25$ ps, defining the Nyquist-limited frequency to $f_{max} = \frac{1}{2dt} = 20$ GHz.

The simulations are performed on a super-cell of 200 replicas of the primitive cell, defining our wavevector resolution to $dk = \frac{2\pi}{200\times a} = 0.123 \times 10^7$ rad/m$\equiv$ 0.0123 rad/nm. The plots that we will show are limited to slightly more than a BZ, enough to recognize, through their dispersion curves, either propagating or stationary modes.

As for the spatial dependence, we adopted a wavevector k_x=0.0490 rad/nm, i.e., twice as large as the BZ. For the temporal dependence, we use

$$b(t) = b_0 \sin(2\pi f_0(t - t_0))/(2\pi f_0(t - t_0))$$

with $b_0 = 1$ mT, cutoff frequency $f_0 = 40$ GHz, and a delay time $t_0 = 50$ ns. Once we recorded the time-resolved 2D profile maps of the magnetization, we apply the Fast Fourier Transform (FFT) in order to obtain the SW dispersion relations [54]. We also determine the SW spatial profiles by performing simulations on a single primitive cell (and no longer on a supercell of 200 copies of it), keeping the previous periodic boundary conditions to mimic the realistic film. This technique limits the results to $k = 0$, hence, we find the profiles as the real part of the FFT coefficients of each micromagnetic cell in the primitive cell. Such profiles must be understood within the Bloch picture, after which the spin wavefunction (i.e., the magnetization fluctuation) in periodic magnetic systems is expressed as [55]:

$$\delta\mathbf{m}_\mathbf{k}(\mathbf{r}) = \delta\tilde{\mathbf{m}}_\mathbf{k}(\mathbf{r})e^{-i\mathbf{k}\cdot\mathbf{r}} \tag{2}$$

where $\delta\tilde{\mathbf{m}}_\mathbf{k}(\mathbf{r})$ is the SW cell function (which extends over the primitive cell and has the periodicity of the system), $\mathbf{k}$ is the wavevector, and $\mathbf{r}$ is the position across the lattice. Hence, the profiles that we will show are the real part of the z-component of the SW cell function (always relevant to the experiments) [56–59].

3. Results and discussion

In this section, we show the results of the micromagnetic simulations concerning the alterations of the film BA and DE dispersion, from a uniform to an undulated magnetization. We recall that the undulation is in the direction of the applied field (magnetic moments in a head-to-tail configuration), namely the x-axis. After unveiling the ultimate physical effect responsible for the opening of the frequency gaps at

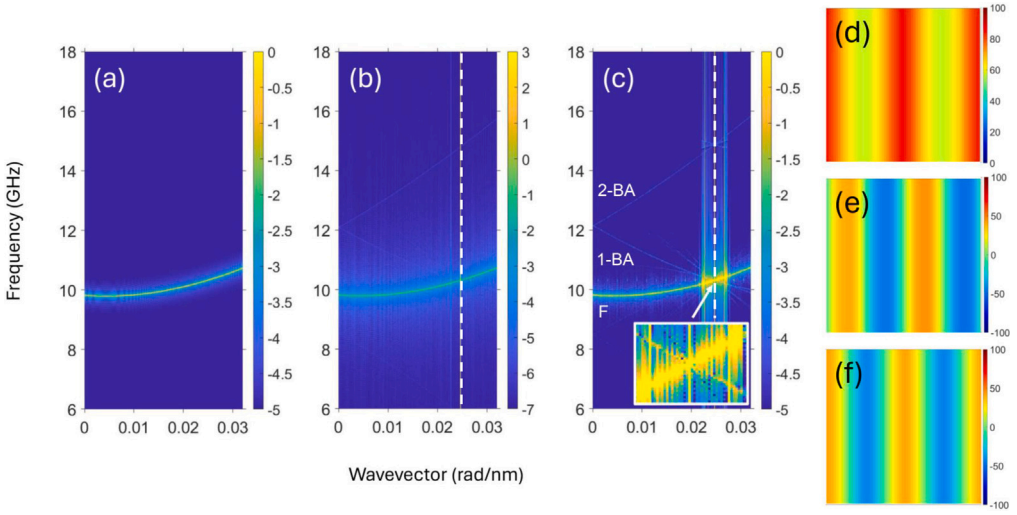

Fig. 3. Magnonic dispersion relations for BA waves in the non-interacting case of a film with in-plane sinusoidal magnetization prepared at different relative amplitude $A = m_y^0/m_x^0$: (a) $A = 0$, i.e., the reference, uniformly magnetized film; (b) $A = 0.2$; (c) $A = 0.5$. Note in (b) and (c) the occurrence of the mirroring to the first BZ due to periodicity, and the remarkable absence of any frequency gap at the BZB, i.e., $k = 0.0245$ rad/nm, as demonstrated in the inset by the crossing of the curves (in the inset the image is magnified and saturated). The color-bar is in arbitrary units, chosen to highlight the tiny lines mirroring in the reduced BZ to prove periodicity. Panels on the right: cell function profiles (real part of the z-component of the dynamic magnetization) of (d) the fundamental (F) mode, (e) the 1-BA mode, crossing the F mode curve at the BZB, and (f) the 2-BA mode. The magnetization undulation underlying these mode profiles qualitatively corresponds to the one shown in Fig. 2(b).

zone boundary, we review the film SW dynamics of the undulated magnetization distributions ensuing the application of either a sine or chiral bias field. In all simulations, we consider an additional uniform field, fixed to 0.1 T throughout this paper. Since the magnetization undulation propagates along a fixed direction (x-axis, Fig. 1), we expect a band structure along this direction only, hence for the BA configuration (corresponding to $\mathbf{k} \parallel \mathbf{M}$) while no periodicity is expected along the other in-plane direction (y-axis, i.e., DE configuration corresponding to $\mathbf{k} \perp \mathbf{M}$). Nevertheless, we will see how the sole existence of periodicity in one direction influences the dynamics in the other, introducing new solutions. For the sake of completeness, we observe here how the other possibility, with the magnetic moments perpendicular to the undulation direction and hence parallel to each other in any direction, would lead to the case of a uniformly magnetized film.

3.1. SW dispersions under an in-plane sinusoidal magnetization distribution: "non-interacting" case

Following the plan of the investigation outlined in Section 2, we prepared an in-plane sine magnetization with period a, with undulation at different relative amplitudes A, and subject to a uniform bias field B_0. However, no relaxation was allowed, nor was any external periodic field introduced; we might address this as the "non-interacting" case. As previously observed, in the simulation we set this distribution as an artificial equilibrium point (ground state) by setting to zero the damping parameter ($\alpha = 0$). The application of an excitation to this artificial ground state will produce small fluctuations around it, which will be solely due to spin-waves.

In Fig. 3 we show the dispersion relations for the cases (a) $A = 0$, (b) $A = 0.2$ and (c) $A = 0.5$. We recall that the direction of the magnetization undulation is parallel to the direction of the wavevector, hence the dispersions refer to the BA mode [50,60]. In thicker films at low k, this volume wave is usually characterized by a negative slope in its dispersion relation, resulting in a negative group velocity. In our case, due to the very small thickness (5 nm), exchange interaction dominates and only a positive slope is observed at low k. Despite being unrealistic because of the vanishing damping, the resulting SW dispersion relations show two interesting features. First, the Brillouin zone boundary (BZB) occurs at $k_{BZB} = 0.0245$ rad/nm, twice the expected value of 0.01225 rad/nm. This means that the actual lattice constant d is a half of the geometric one a, and hence that the SW dynamics is invariant after a mirror operation σ_h in the magnetization (across the horizontal axis, namely a change of sign of m_y component) [61]. As a consequence, the BZB wavevector is $k_{BZB} = \pi/d \equiv 2\pi/a = 0.0245$ rad/nm. Second, no gap arises at the zone boundary, independently of the relative amplitude A. This is shown in the inset of Fig. 3(c), where the dispersion of the fundamental mode F is crossed by its reflection, 1-BA, with opposite group velocity. Given that the bias field is uniform, the modes responsible for the dispersion curves at the BZB are invariant for translations of a half period ($d/2$) [60]. The cell function ($k = 0$) of these SW modes is shown in Fig. 3. In panel (d) we show the fundamental mode (F), occurring at 9.81 GHz; in panel (e) we show the backward mode with 1 nodal line in the cell function (1-BA), occurring at 12.2 GHz; and in panel (f) we show the 2-BA mode, almost degenerate in frequency with the 1-BA. Following Eq. (2), at the BZB the F and 1-BA modes are indistinguishable and hence degenerate in frequency because the medium is continuous and homogeneous, and only a uniform field is applied. Of course, when dot or antidot lattices are concerned, or even multi-material systems [62], the two modes cannot be degenerate and a gap opens. In fact, in the next section, we illustrate in detail how the band-gap arises as a consequence of translational symmetry breaking, attained by introducing a sinusoidal bias field with period a ("interacting case"). We recognize here how periodicity is a necessary, but not sufficient, condition for the opening of a gap [63].

It is interesting to observe how the crossing of the dispersions of the F and 1-BA modes at the BZB occurs in a linear form, which is reminiscent of the behavior of topological Dirac magnons [64–66] with a gapless metallic behavior, which will be the subject of a future investigation.

3.2. "Interacting" case: Relaxation to in-plane periodic bias fields

As mentioned in the investigation plan, a more realistic approach to obtain a sinusoidal magnetization is to relax an initial uniform magnetization to a bias periodic field B_P, in addition to the uniform field, $B_0 = 0.1$ T, with $B_P/B_0 \leq 1$. We will apply a sine oscillation ($B_P \equiv B_S$) and then a chiral oscillation ($B_P \equiv B_C$) [Fig. 2 (a, c)]. It helps recalling that the fan angle is partial in the former, $\theta_F = \pi/2$, while it is complete in the latter, $\theta_F = 2\pi$. In both cases, we consider

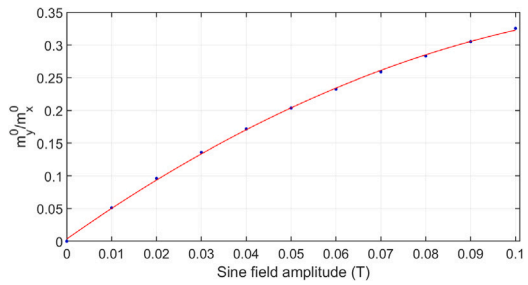

Fig. 4. Relative amplitude $A = m_y^0/m_x^0$ between the y and x components of the magnetization at $x = 0$ as a function of the B_S magnitude (in tesla). The red line is a guide for the eye. For a correspondence with Fig. 3, we obtain $A = 0.2$ for $B_S = 0.0227$ T and $A = 0.5$ for $B_S = 0.06$ T.

an in-plane field oscillation, namely $B_P = B_P(x, y)$, which influences the resulting magnetization distribution, and must be thought of as the simulation of the vertical interaction with another layer in the context of 3D Magnonics. The application of a B_P with a given magnitude and symmetry determines the relative amplitude of the equilibrium magnetization distribution and, hence, the fan angle of $M(x, y)$. Given that B_P is a bounded function, the sum vector $\mathbf{B}_{\text{tot}} = \mathbf{B}_P + \mathbf{B}_0$ possesses a fan angle that is always smaller than the vector $\mathbf{B}_P$ alone, and for this reason, the apparent amplitude of the resulting magnetization oscillation (Fig. 2 (b, d)) will appear less pronounced compared with the corresponding sine or chiral fields (Fig. 2 (a, c)).

Note that in this case we did compute a relaxed, equilibrium magnetization prior to excitation: hence, we had to use a non-vanishing damping parameter α. However, in order to both attain the equilibrium magnetization and get (in reasonable times) clear-cut dispersion curves we used 1% of the real damping (i.e., we used $\alpha = 0.0001$), to attain long lasting precession, and consequently larger Fourier coefficients. We remark that in the linear (low power) regime the damping parameter has no role in determining the relationship between frequency and wavevector, but only to attenuate and possibly broaden the intensity of the corresponding curve at high k[62,67,68].

3.2.1. Sine-field

First we investigate the effects on the SWs of a periodic sinusoidal field, $B_P \equiv B_S$. As shown previously, after relaxation the magnetization varies along the x-direction as a sine function with amplitude $Y_0 \propto A$. The relative amplitude A of the magnetization undulation as a function of the magnitude of B_S is plotted in Fig. 4, so that it is possible to trace a correspondence with the cases of the previous section, where only A was given.

The resulting SW dispersion curves, as a function of the magnitude of B_S, are shown in Fig. 5. In general, we recognize how the frequency increases with the magnitude of B_S, namely as the undulation amplitude of the magnetization increases. In fact, by increasing B_S, the overall bias field (superposition of $B_S(x, y)$ and B_0) increases too, therefore the Zeeman potential energy increases making the magnetization stiffer with respect to deflections from the equilibrium point; consequently the frequency (at a given k) increases too. This effect is general, hence independent of the propagation direction of the wave. Consequently, this is also seen for DE waves shown in Fig. 6. As in the previous case, where no sine-field is present, the dynamics is invariant with respect to the change of sign of the component m_y, and the unitary primitive cell corresponds to half the geometric one, with lattice constant $d = a/2$. Hence, the BZB occurs at $k_{BZB} = \pi/d \equiv 2\pi/a = 0.0245$ rad/nm (Fig. 5).

In contrast to the previous *non-interacting* case, here a frequency gap arises at the BZB for sufficiently large B_S magnitudes. The two spin-wavefunctions F and 1-BA [Fig. 7(b,c)] are no longer invariant in frequency (energy) because of the presence of the sinusoidal bias field B_S with period a. As a consequence, here we demonstrate that the frequency gap is the result of the dynamic interaction with the vector field $B_S(x, y)$ that causes the undulation.

The genesis of the frequency gap is the following. Due to Bragg diffraction, two stationary wavefunctions form at the zone boundary, one with nodes in correspondence to the nodes of the sine-field (i.e., at $d = a/2$), the other with nodes in correspondence to the maxima of the sine-field (i.e., at $d/2 \equiv a/4$). This is illustrated in Fig. 8. Then, the two waves react to the field B_S in different ways, the former achieving the lowest frequency (the top of the lower band), the latter the highest frequency (the bottom of the upper band), hence producing a visible frequency gap (inset of Fig. 5(c)). Conversely, in Fig. 3, there is no gap at the zone boundary (degeneracy): in such a case, the absence of the non-uniform sine-field B_S restores a translational symmetry and hence an invariance with respect to translations of $d/2$, such that it is not possible to discriminate between the wavefunction of either the F or the 1-BA mode (shown in Fig. 3(d) and (e)). As the undulation amplitude increases, the discrepancy between the direction of each magnetic moment and the overall bias field $\mathbf{B}_S + \mathbf{B}_0$ increases, particularly at the center and the ends of the primitive cell, hence the energy difference between the two modes F and 1-BA increases, i.e., the frequency gap increases (Fig. 9). More precisely, starting from $B_S = 0$, and with increasing B_S, the y component of the magnetization progressively increases in correspondence to B_S nodes (i.e., at $x = 0, a/2, a$), but remains almost vanishing in correspondence to the crests (zero derivative, at $x = a/4$ and $x = 3a/4$). In other words, the average angle θ_k formed by the local magnetization and the propagation direction (x) is increasingly larger in the first regions, where 1-BA has maxima, but almost constant in the second ones, where instead it is the F mode to have maxima. This makes the corresponding frequencies increasingly different (as is understandable, for example, by using the so called Herring–Kittel formula [69] or the corresponding one for thin films [70]). Hence, as B_S increases, the transverse component of the magnetization m_y follows suit, causing the gap to increase. This increase is found to be linear up to $B_S = 0.03$ T, then going to saturation. Apparently, after some critical m_y, the energetic difference between the two regions stops increasing as it reaches saturation. By linear interpolation we estimate the increasing rate (up to $B_S = 0.03$ T) around 5.00 rad GHz/T.

The profiles of the Bloch waves providing the dispersion of Fig. 5(b), with $B_S = 0.03$ T, are shown in Fig. 7: panel (a) corresponds to the lowest frequency dispersion curve (fundamental mode), panel (b) to the 1-BA mode, responsible of a negative dispersion curve that terminates in a gap at the BZB, and panel (c) to the 2-BA mode, almost degenerate with the 1-BA at $k_x = 0$ but showing a positive slope in the dispersions. These curves are very similar to the non-interacting case (B_S=0) of Fig. 3.

Furthermore, we determine how the presence of the periodicity in one direction (x) influences the dynamics in the other perpendicular direction (y). This is a direct consequence of the Bloch theorem: due to periodicity, the dispersion along k_x folds to the reduced BZ, intercepting the $k_x = 0$ axis in many points. Hence, while a uniform film has a single solution at $k_x = 0$, a periodic system has many solutions (higher order modes, labeled as F or 0-BA, 1-BA, 2-BA, 3-BA etc.). Each of these new solutions correspond to a different cell function for a new Bloch wave (Eq. (2)) traveling also along the perpendicular direction (y-axis), and showing a single-valued dispersion curve in analogy with the magnetostatic wave dispersions in uniformly magnetized films. Along y-axis no periodicity is present, which justifies why only single-valued curves are found. This is valid also for the xz-polarization (Section 3.2.3). Hence, periodicity along x creates multiple spin-wave degrees of freedom also along y, visible as multiple dispersion curves.

3.2.2. Chiral field

The application of a chiral field $B_C(x, y)$ [Fig. 2, panel (c)] to a film with saturated magnetization breaks the mirror symmetry mentioned in the previous case, so that now the physical primitive cell coincides

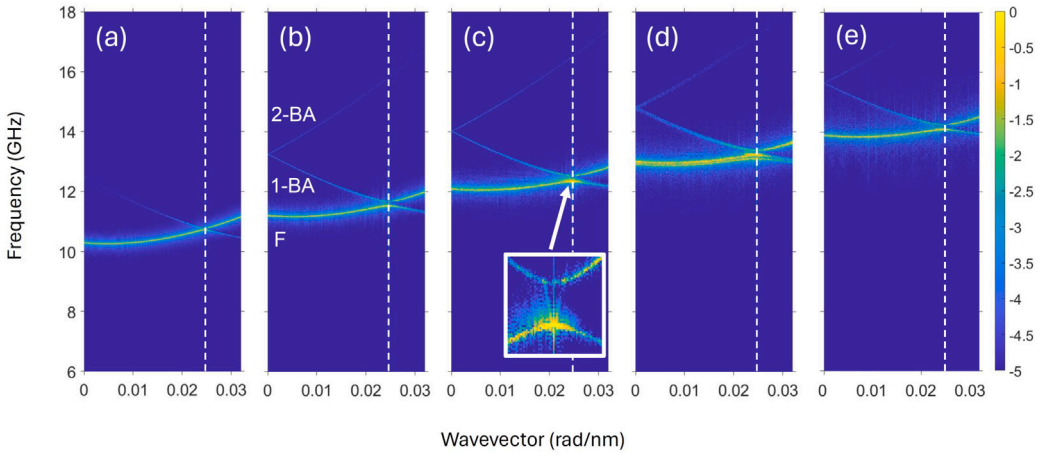

Fig. 5. Magnonic dispersion curves for BA waves at different values of the sine field magnitude B_S (polarization in the xy plane). Panel (a): 0.01 T. Panel (b): 0.03 T. Panel (c): 0.05 T. Panel (d): 0.07 T. Panel (e): 0.09 T. In (c) the inset highlights by magnification the opening of a gap at the BZB.

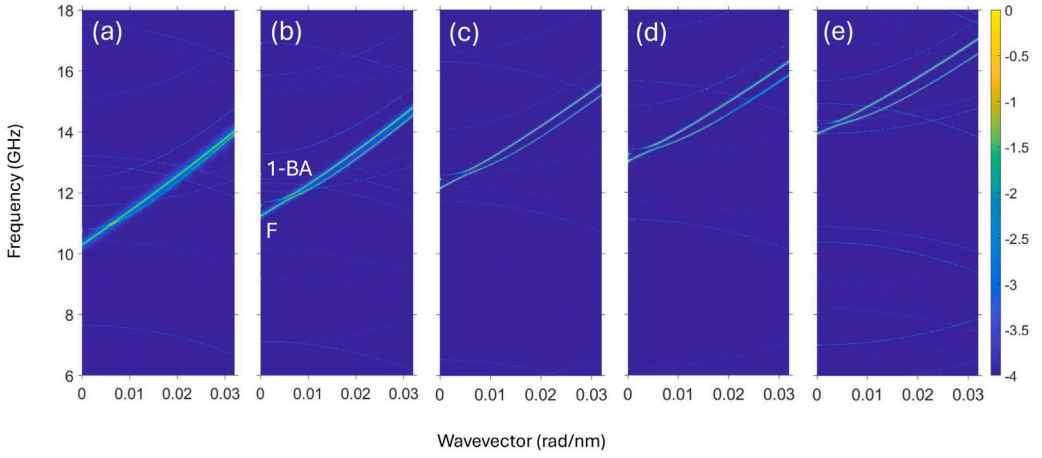

Fig. 6. Magnonic dispersion curves for DE waves (intensity in arbitrary units) at different values of B_S (polarization in the xy plane). Panel (a): 0.01 T. Panel (b): 0.03 T. Panel (c): 0.05 T. Panel (d): 0.07 T. Panel (e): 0.09 T.

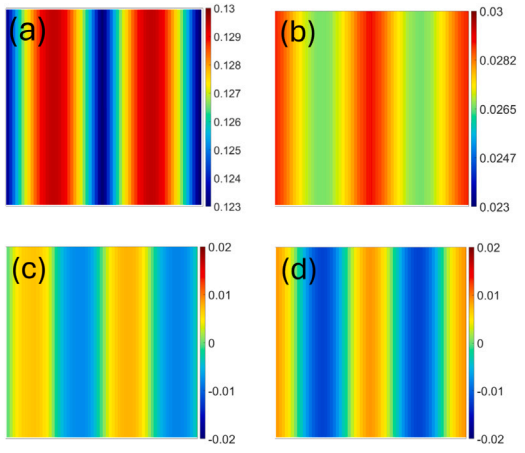

Fig. 7. (a) Effective field B_{eff} profile for in-plane polarized magnetization at B_S = 0.03 T (color bar in tesla). (b-d) Real part of the out-of-plane (z) component of the dynamic magnetization at $k = 0$ at the frequencies giving non-vanishing signal in the dispersions at B_S = 0.03 T: (b) F-mode (11.13 GHz); (c) 1-BA mode (13.14 GHz); (d) 2-BA mode (13.14 GHz). Intensity in arbitrary units. The magnetization undulation underlying these mode profiles qualitatively corresponds to the one shown in Fig. 2(b).

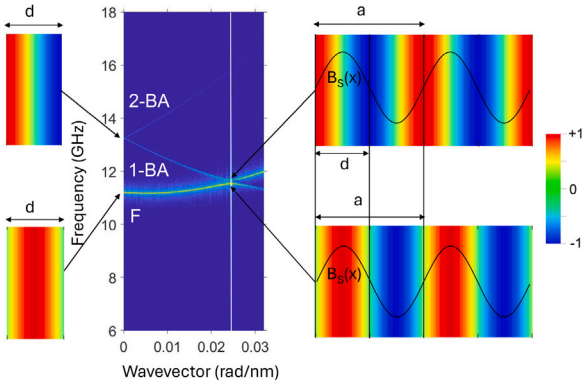

Fig. 8. Illustration of the origin of the frequency gap at the BZB: at the center, the (indicative) dispersion diagram taken from panel (c) of Fig. 5. On the left, the mode profiles F and 1-BA at $k = 0$, referred to the actual primitive cell which is demonstrated to be $d = a/2$. On the right, the two reconstructed profiles (colors in arbitrary units) as must appear at the BZB following Eq. (2), superimposed to the sine-field $B_S(x)$ (black curves) which has a period a. at the BZB the two wavefunctions F and 1-BA differ only for the translation of $a/4 \equiv d/2$ and lead to the emergence of the frequency gap because of the different phase relationship with $B_S(x)$.

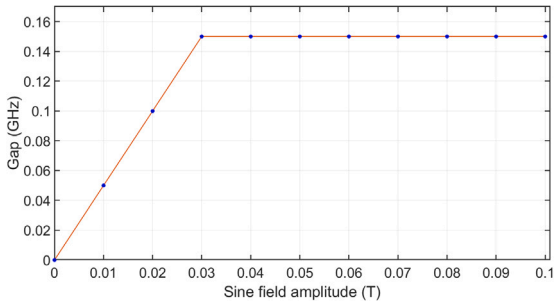

Fig. 9. Evolution of the frequency gap as the magnitude of the sine field B_S (in tesla) is varied (magnetization in xy plane). Blue dot: data. Red line: linear fit ($y = 5x$ in the range [0, 0.03 T], then $y = const = 0.15$).

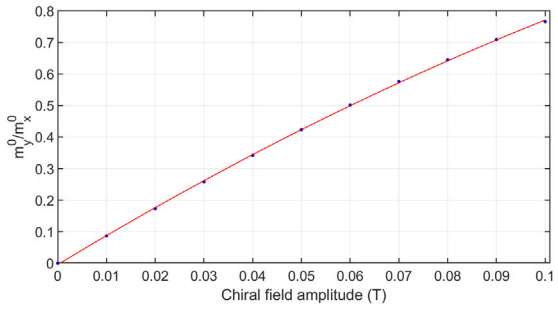

Fig. 10. Relative amplitude $A = m_y^0/m_x^0$ between the y and x components at $x = 0$ as a function of the B_C magnitude (in tesla). The red line is a guide for the eye.

with the geometric one (i.e., the lattice constant is a). The change of sign of component B_C^x, a turning point occurring at $a/2$, divides the primitive cell into two nonequivalent regions. Since the x-component of B_C is always smaller or equal to that of B_0, its change of sign is unable to modify the corresponding m_x component, hence it is unable to produce a likewise chiral magnetization, but is very effective in determining a larger demagnetizing field in the second half of the primitive cell because of its antiparallel orientation. This fact, together with the persisting negative component m_y across the turning point, allows the magnetization flux to complete its sinusoidal shape, though with a curvature more pronounced than in the first half. As we will see, this asymmetry transfers to the effective internal field and, as a consequence, to the SW dynamics (mode profile and frequency).

In Fig. 10 the ratio $A = m_y^0/m_x^0$ of the magnetization components taken at position $x = 0$ is shown as a function of B_C for direct comparison with the analog Fig. 4. In the first part of the primitive cell, both the average chiral field and magnetization vectors point in the same direction, so they can be compared. Because of the larger fan angle inherent to the chiral field, the magnetization relative amplitude A is larger than in the case with the sine field B_S.

In Fig. 11 we show the evolution of the dispersion curves as the chiral field magnitude B_C is increased. In the figure, more than a BZ is included to recognize both stationary and propagating modes. The first observation to such dispersions is that the BZ boundary occurs at $k_{BZB} = \pi/a \equiv 0.01225$ rad/nm, consistently with the fact that now the physical primitive cell coincides with the geometric one. In analogy to what happened with B_S, even here, as B_C is increased, we see that the dispersion structures gradually shift to higher frequencies. Ultimately, B_C is an additional bias field, as B_S was, and its increase results in an increase of the overall Zeeman interaction, and consequently a general frequency increase [5]. As is apparent from the dispersions, at a given value of the magnetic field, the frequency increase is smaller if a chiral field is applied rather than a sine. In fact, the dipolar (demagnetizing) fields are on the average higher when a chiral field is applied, and these higher dipolar fields are known to contrast the Zeeman interaction and hence hinder the overall frequency increase [70–72].

In contrast with the previous sine-field case, here we see the occurrence of a flat dispersion (i.e., a stationary mode) even at low B_C values, the first one occurring at around 9.5 GHz when $B_C = 0.01$ T [Fig. 11, panel (a)]. Not only does its frequency tend to decrease as B_C is increased but also the number of flat dispersions increases with increasing B_C. These features, distinctive of the chiral field, can be understood in light of B_{eff} (Fig. 12, panel (a)). First, departing from the previous case, when a chiral field is applied, B_{eff} loses the mirror symmetry σ_v [61] and, in the right-side of the primitive cell, reaches a deep absolute minimum, acting as a well for SWs. Hence, even at low B_C values, the lowest frequency mode happens to localize within such a well, its spin-wavefunction fast decaying outside it [Fig. 13, panel (a)]. The localization of the lowest frequency mode in the minimum of B_{eff} [Fig. 12, panel (a)] is a well known effect [13,73–78]. Due to the strong localization (i.e., the limited extension) its stray (dynamic) coupling fields are too small to determine a significant bandwidth, and the mode happens to be stationary (zero group velocity $v_g = \partial\omega/\partial k$) [77]. Moreover, as B_C is increased, B_{eff} becomes increasingly deeper (Fig. 12(b)) on the right-side of the primitive cell, where magnetization and chiral field are antiparallel. From one side, this allows the well to host more localized modes, determining more flat dispersions. From the other, this justifies the progressive frequency decrease of such localized mode with increasing B_C, as appearing in the dispersions.

The dependence of this localized mode on B_C is shown in Fig. 14: from linear interpolation, we found a slope $\frac{df}{dB}$=-35.2 GHz/T, from which we get the effective gyromagnetic ratio [14]:

$$\gamma_{\text{eff}} = 2\pi \frac{df}{dB} = -221 \text{ rad GHz/T}, \tag{3}$$

significantly larger than the permalloy material (185 rad GHz/T). The negative value is an indication of the increasing instability of the magnetization on the right-side of the primitive cell, since locally chiral field and magnetization are antiparallel. Remarkably, the periodicity of the magnetization provides our film with effective properties like γ_{eff}, which the material itself does not possess: this aspect is typical of meta-materials, which display enhanced properties arising from the designed structure [79]. The possibility of engineering γ_{eff} by a considerate design of the magnetization distribution is particularly attractive in the perspective of making indirect measurements of magnetic field variations, for new generation sensing devices [80–82].

We remark upon the importance of having, in a single system, more solutions within few 100 MHz with opposite dynamic behavior (stationary vs. propagating) but with cell functions with compatible symmetry [(b) and (c) in Fig. 13]. In fact, in such conditions, the same antenna can excite one or the other merely by implementing a small frequency shift. As a consequence, information can be easily stored or delivered on the same physical device in real time. Our results showed precisely how the application of a chiral field provides a ferromagnetic film with this property.

3.2.3. *Out-of-plane magnetization oscillation*

We apply the relaxation approach to compute the dispersions in a film with an out-of-plane oscillation of the magnetization (i.e., polarized in the xz-plane), extending along the x-axis. Such an undulation is created after the application of a sine field B_S with similar polarization and modulation, to which the magnetization relaxes. We consider again both BA and DE waves, the dispersions of which are shown in Figs. 15 and 16, respectively. Clearly, the periodic structure is perceptible only for BA waves, while DE waves behave like plane waves in a homogeneous medium. However, again the folding of the BA dispersion to the reduced BZ introduces new solutions even for the DE waves, in particular the DE wave with a 1-BA cell function, visible in the dispersions as an additional sister curve intersecting the $k = 0$ ordinate at higher frequency. We remark how, in principle, any DE wave with a

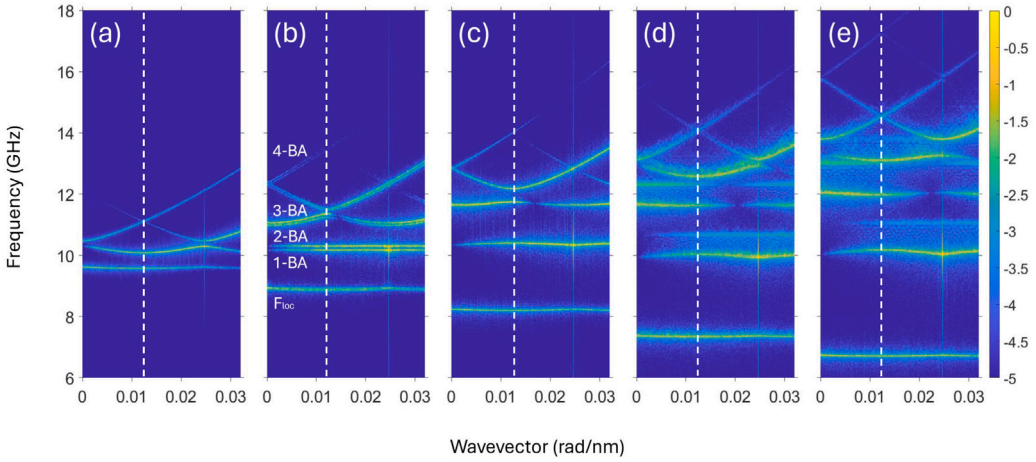

Fig. 11. Magnonic dispersion curves for BA waves at different values of the chiral field B_C. Panel (a): 0.01 T. Panel (b): 0.03 T. Panel (c): 0.05 T. Panel (d): 0.07 T. Panel (e): 0.09 T. Note that, due to a reduced magnetization symmetry, when a chiral field is applied the BZB occurs at $k_x = 0.01225$ rad/nm.

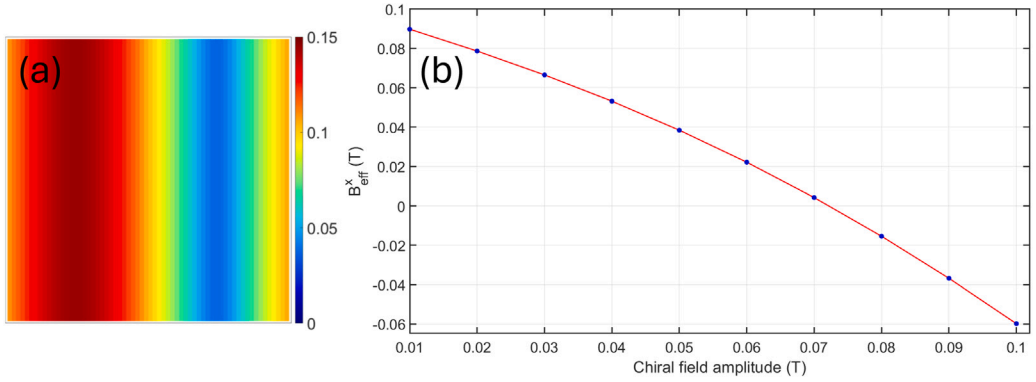

Fig. 12. (a) B_{eff} along the x direction (color bar in tesla) when $B_C = 0.05$ T, and (b) its behavior as a function of the chiral field amplitude (magnetization undulation polarized in the xz plane, BA configuration). The red line is a guide for the eye.

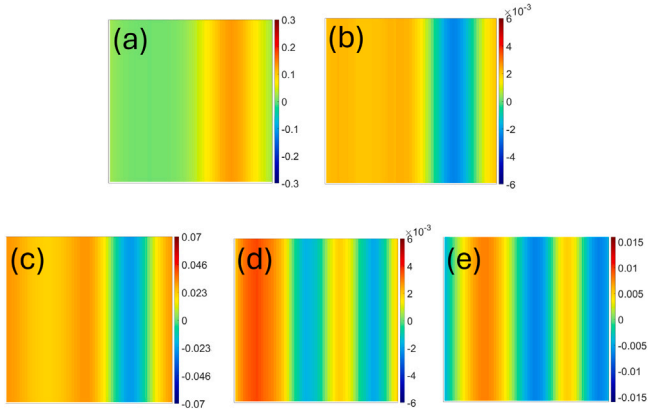

Fig. 13. Real part of the out-of-plane (z) component of the dynamic magnetization at $k_x = 0$ at the frequencies giving non-vanishing signal in the dispersions. For $B_C = 0.05$ T: (a) localized F-mode F_{loc}, 8.23 GHz; (b): 1-BA mode, 10.34 GHz; (c): 2-BA mode, 11.58 GHz; (d) 3-BA mode, 13.17 GHz; (e) 4-BA mode, 13.17 GHz. The magnetization undulation underlying these mode profiles qualitatively corresponds to the one shown in Fig. 2(d).

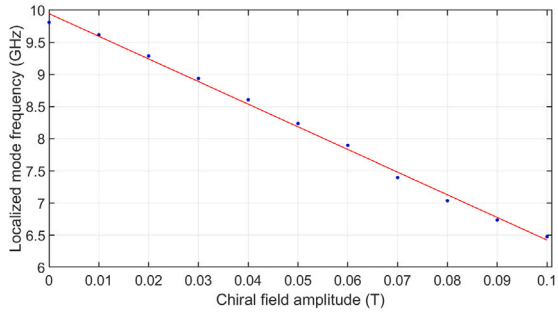

Fig. 14. Evolution of the frequency of the localized mode as the magnitude of the chiral field B_C is varied (magnetization undulation polarized in xy plane). Blue dot: data. Red line: linear fit ($y = -35.2x + 9.9$).

n-BA ($n > 1$) cell function profile creates its dispersion, though with an intensity rapidly decreasing with increasing n. In addition, we observe how the slope of the DE-dispersion is much larger for an out-of-plane undulation (Fig. 16) than for an in-plane one (Fig. 6). This might be ascribed to the different orientation of the magnon wavevector with respect to the polarization plane of the magnetization undulation, despite the fact that **k** is always along y-axis. However, in the in-plane case, **k** lies within the polarization plane of the magnetization and hence is properly in the DE configuration; in the out-of-plane case, **k** is perpendicular to the polarization plane of the magnetization, hence, more appropriately, in the configuration of forward volume SW modes (FVSWM). In uniformly magnetized films, in general, the slope of the SW dispersion for FVSWM is larger than for DE modes, due to the different effects of the demagnetizing field [83].

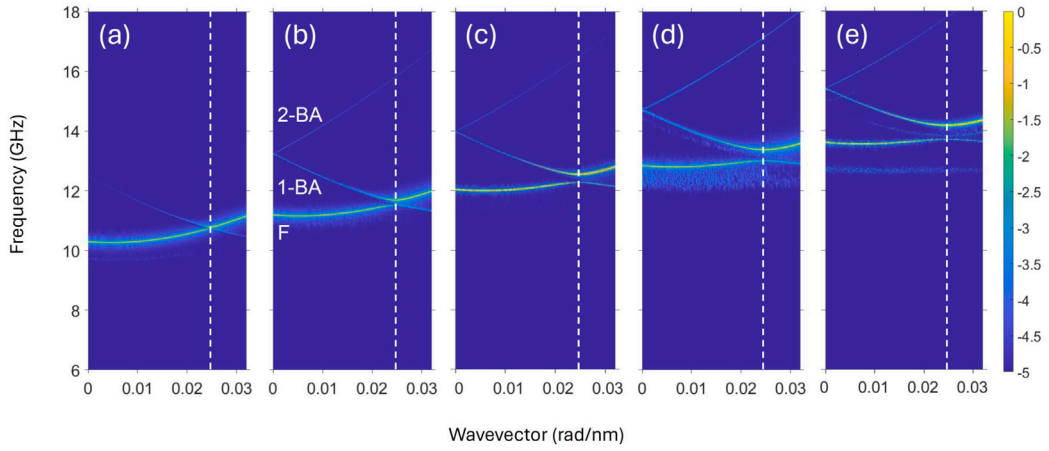

Fig. 15. Magnonic dispersion curves for BA waves at different values of the sine field B_S polarized in the xz plane. Panel (a): B_S=0.01 T. Panel (b): B_S=0.03 T. Panel (c): B_S=0.05 T. Panel (d): B_S=0.07 T. Panel (e): B_S=0.09 T.

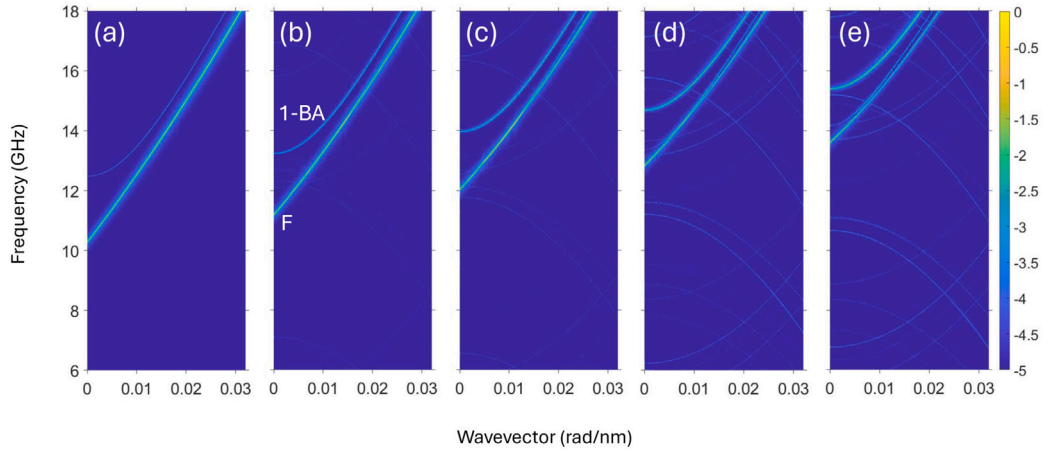

Fig. 16. Magnonic dispersion curves for DE waves at different values of the sine field B_S polarized in xz plane. Panel (a): B_S=0.01 T. Panel (b): B_S=0.03 T. Panel (c): B_S=0.05 T. Panel (d): B_S=0.07 T. Panel (e): B_S=0.09 T.

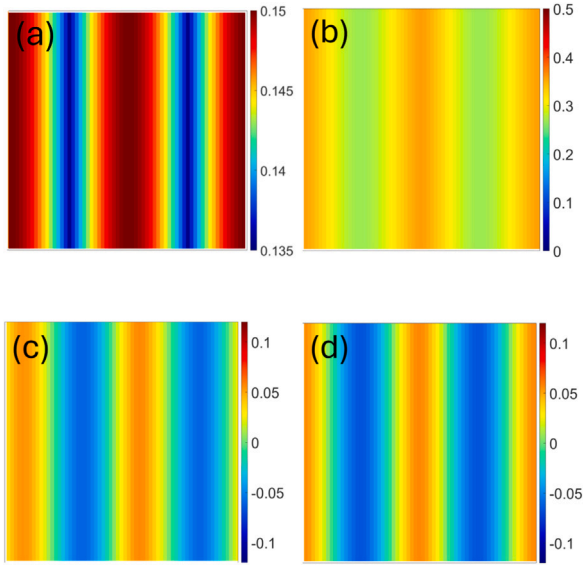

Fig. 17. (a) Space profile of the x-component of B_{eff} when B_S = 0.05 T, where the color bar units are in tesla; (b-d) Spatial profiles, in arbitrary units, of the modes giving the dispersions of Fig. 15(c) with B_S=0.05 T (magnetization undulation polarized in xz plane, BA configuration): (b): FM (12.03 GHz); (c): 1-BA mode forming a gap at the BZB with the FM (13.97 GHz); (d): 2-BA mode (13.97 GHz).

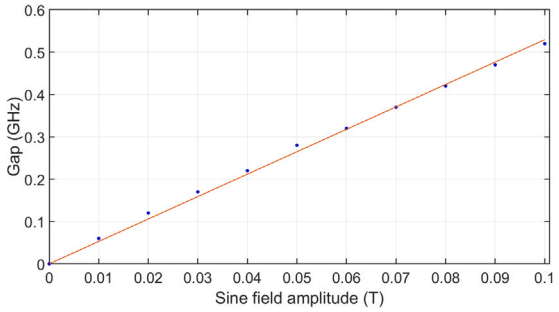

Fig. 18. Evolution of the gap as the magnitude of the sine field B_S is varied (polarization in xz plane). Blue dot: data. Red line: linear fit ($y = 5.3x$).

The profiles responsible for the dispersion curves of the out-of-plane case are shown in Fig. 17, and display similarities to those presented for the in-plane case of Section 3.2.1. First and foremost, the fundamental (F) mode, characterized by an in-phase amplitude (no phase changes) all across the primitive cell, though with larger values in correspondence to the nodes of the sine-field $B_S(x)$: this follows the pattern of B_{eff} (panel (a)). The F mode produces the most intense curve with a positive slope in both BA and DE configurations.

The 1-BA and 2-BA modes are responsible for the folding of the dispersion to the reduced BZ along the direction x. As commented

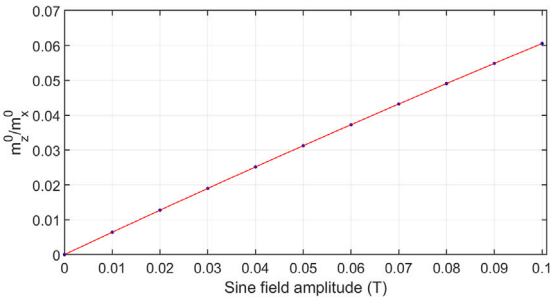

Fig. 19. Relative amplitude $A = m_z^0/m_x^0$ between the z and x components of the magnetization at $x = 0$ as a function of the out-of-plane B_S magnitude (in tesla). Here B_S is polarized in the xz plane. The red line is a guide for the eye.

above, the 1-BA mode is also responsible for the second most intense curve in the DE configuration, where $\mathbf{k} \perp \hat{\mathbf{x}}$ (Fig. 16).

Similarly to the in-plane case, a frequency gap is formed at the BZB as B_S is increased. The dependence of such a gap on the applied sine field $B_S(x, z)$ is shown in Fig. 18. Curiously, in contrast with the in-plane case, the curve does not saturate, but keeps its linear trend independently of B_S. This can be ascribed to the limited increase of the transverse magnetization component m_z of the out-of-plane case, with respect to m_y of the in-plane case, limiting the energetic difference between the complementary zones of the primitive cell where F and 1-BA modes have their maxima (see Section 3.2.1). Due to the reduced thickness of the film, the very strong demagnetizing fields limit the increase of the out-of-plane component m_z of the magnetization for any given applied B_S. This was determined by comparing Fig. 4 with Fig. 19: at a given B_S the relative amplitude in the present out-of-plane case is around one order of magnitude less than in the in-plane case. Evidently, the critical value of the transverse magnetization component is hardly reached when this component has to align along the thickness of the film, because of the strong dipolar fields. As a consequence, the curve does not saturate. From a linear interpolation we found the (average) increasing rate about 5.30 rad GHz/T, which is close to the one found in the in-plane case (where it was limited to the interval [0, 0.03 T] before saturation) and represents a good validation of the proposed theory. Once more, the linear sensitivity of the gap to fine changes of the applied B_S is clearly attractive for sensing activity [81,82].

In summary, in a system with undulated magnetization, the progressive increase of B_S, in either in-plane or out-of plane geometry, results in a general increase both of the dispersion curves and the frequency gap at the BZ boundary. The increase of the gap is associated with the increase of the transverse component of the magnetization, through its relative amplitude A. Instead, in contrast with the chiral case, in either in-plane or out-of-plane case, no evidence for any localized modes was found.

4. An example of implementation of the sinusoidal field: a periodic inverse-magnetoelastic interaction

In this Section we show how it is possible to generate a continuous sinusoidal field through a discrete set of domains of a variable physical quantity. In our practical implementation, the physical quantity is the ferroelectric (FE) domain polarization in a FE layer, which can be oriented in different directions thanks to a periodic succession of stripes of different lattice elongation, forming the FE layer. Then, the polarization intensity can be tuned by an electric field of appropriate magnitude and direction, having the periodicity of the FE stripes [84,85]. Through inverse magnetostriction (i.e., the vertical coupling), the FE polarization induces in the ferromagnetic underlayer a likewise discrete set of magnetic anisotropy domains with varying easy axis. This effect was reproduced in real samples in Ref. [86–88], where it was shown how a multiferroic heterostructure, consisting of a structurally continuous ferromagnetic film on a ferroelectric $BaTiO_3$ substrate with ferroelastic stripe domains, was able to cause the imprinting of a ferromagnetic stripe pattern by strain transfer at the interface of this hybrid structure. The strong polarization of the FE domains produced a pattern which was characterized by 90° rotations of a (strong) uniaxial magnetic anisotropy at ferroelectric boundaries, so forming magnetic domains (no sinusoidal magnetization). Experimental details can be extensively found in those papers. In the following, we demonstrate that alternating domains with a small enough magnetic anisotropy can produce a smooth, continuous sinusoidal magnetization. Inspired by the experimental papers cited above, we adopt a similar framework, but aim to reduce the FE/FM strain-mediated-vertical coupling (e.g., by tuning the applied electric field magnitude and direction), so to reduce the magnetic anisotropy coefficient until a continuous sinusoidal distribution is obtained.

In our simulations, we considered a uniform magnetic anisotropy coefficient K_u but four different easy axis directions in four identical regions in the primitive cell: 45°, 0°, -45°, and 0°. The corresponding sketch of the periodic domain distribution is shown in Fig. 20(a). We also apply a uniform bias field $B_0 = 0.1$ T, in analogy to what done in Section 3.2. We found that if $K_u \geq 40$ kJ/m^3, magnetic domains form in perfect correspondence with the FE domains, with a discontinuity of $\partial M/\partial x$ across each domain wall (Fig. 20(b)): this is clearly outside our interests. In contrast, if $K_u < 40$ kJ/m^3, the magnetization relaxes in a continuous sinusoidal distribution (Fig. 20(c)). The upper limit value of K_u was found to be strictly dependent on the applied uniform bias field: larger bias fields would delay the formation of magnetic domains, allowing sinusoidal distributions even at higher K_u. For this reason, we chose a low value $K_u = 10$ kJ/m^3 for our investigation and computed the frequency-wavevector curves. The results are shown in Fig. 20(d), where the distinctive folding of the dispersion curve to the reduced Brillouin zone, as well as the frequency gap at the BZB. These results are qualitatively similar to those predicted by the more general approach of the in-plane sinusoidal field (Fig. 5). Hence, we demonstrated that it is possible to implement a sinusoidal field by vertical coupling with a discrete arrangements of domains of a given physical quantity (in our case, the magnetic anisotropy as a simulation of the inverse magnetostriction).

5. Conclusions

We devised an original method to control the SW propagation along a ferromagnetic film by manipulating the spatial undulation (amplitude and symmetry) of its magnetization. First, we recognized the frequency gaps, occurring after the introduction of the periodicity, as the result of the interaction between the SW modes and the magnetic field causing the non-uniform magnetization. This cause can be represented by a vertical or interfacial interaction in any multilayer system, where the sinusoidal distribution is conveyed by an overlayer of appropriate symmetry (macrospin chains, artificial spin ice, DMI, or even ferroelectric domains in multiferroics). To implement the dynamic interaction, we introduced a sinusoidal magnetic bias field B_S, in addition to the uniform one B_0 to which the magnetization relaxes into a sinusoidal distribution. The amplitude of such a sinusoidal distribution can be finely tuned by the magnitude of the sinusoidal field. The interaction of the SW modes with the sinusoidal field produced frequency gaps, which can be varied in magnitude and frequency range by appropriately tuning the sinusoidal bias field magnitude. From the dynamic point of view, the physical primitive cell is half of the geometric one, because the orientation of the crest of the magnetization is seemingly ineffective, only the differential absolute value counts. We also considered the magnetization resulting after relaxation to a chiral field. In this case, the primitive cell divides into two inequivalent halves, one where the magnetization and chiral field are, on average, parallel,

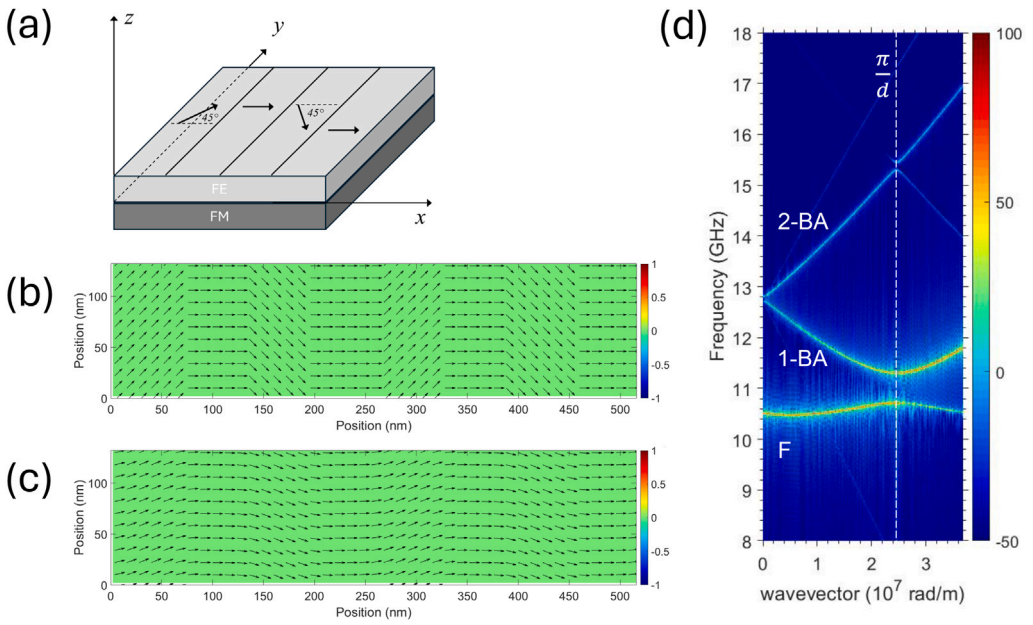

Fig. 20. (a) Sketch of the FE domain distribution in the FE/FM bilayer. Despite discrete, the domains induce a continuous sinusoidal field and hence a continuous sinusoidal magnetization. In (b) we show the formation of magnetic domains when $K_u = 5 \cdot 10^7$ J/m^3; in (c) we show the formation of a sinusoidal magnetization, after relaxation, when $K_u = 40$ kJ/m^3 (this high value allows a visible undulation). In (d) the dispersion curves are shown for $K_u = 10$ kJ/m^3, qualitatively similar to those shown in Fig. 5, with the characteristic folding of the dispersion curve to the reduced Brillouin zone and the formation of a frequency gap at zone boundary.

and the other almost antiparallel. In the second half, the demagnetizing interaction is much larger, due to the larger magnetization divergence, and this determines a deeper effective field where low frequency SWs localize. This asymmetry reflects also in every magnon space profile. In particular, even at a small B_C, an additional solution is found at low frequency values, which is uniform but localized within this second half of the primitive cell. Interestingly, its frequency decreases with increasing B_C, but its dispersion is always flat, hence this mode is localized and stationary independently of the value of B_C. Localized modes are impossible in films with uniform distributions and not found after the application of a sinusoidal field. Their presence was found only after the application of a chiral field: being simultaneous to the propagating ones, with a similar symmetric profile, and just at a few MHz from them, these localized modes provide an additional channel to store and sort dynamic information (i.e., a waveguide can be switched into a dynamic memory without changing the physical ferromagnetic system). Furthermore, we found that the effective gyromagnetic ratio of this localized mode is larger than the one of FMR in permalloy, and this is interesting for designing new generation magnetic sensors.

In conclusion, we conceived and characterized a system where the spin-wave propagation properties can be altered on demand by finely tuning the amplitude of the sinusoidal spatial distribution of the magnetization. This achievement is particularly interesting in the field of 3D-Magnonics, where any appropriate macrospin distribution, magnetic domains or possibly ferrolectric domain orientations in a layer, can convey, by vertical interaction, such a sinusoidal distribution in the magnetization of the film layer underneath. We demonstrated this point by introducing a periodic variation of the magnetic anisotropy easy axis within the primitive cell, in discrete domains of width 64 nm, as a simulation of the inverse magnetoelastic interacton with a ferroelectric layer: at a coefficient K_u below some limit value, the relaxed magnetization was found in a continuous sinusoidal equilibrium state, producing a magnon dispersion similar to what found in the general case with the direct application of a sinusoidal field. The ultimate purpose of the present research is not only to shed light on the complexity of the dynamics in 3D magnonic architectures, but also to provide and characterize new degrees of freedom for signal filtering and manipulation, as well as information storage and delivery. Furthermore, the enhanced properties arising from the sinusoidal distribution (e.g., the effective gyromagnetic ratio) make our system an excellent meta-material candidate for sensing activity. For these reasons, we hope we raised interest on the subject and spur its practical realization with dedicated experimental investigations.

CRediT authorship contribution statement

P. Micaletti: Writing – review & editing, Investigation. **A. Roxburgh:** Writing – review & editing. **E. Iacocca:** Writing – review & editing, Methodology, Conceptualization. **M. Marzolla:** Writing – review & editing, Software. **F. Montoncello:** Writing – review & editing, Writing – original draft, Supervision, Software, Resources, Methodology, Investigation, Funding acquisition, Formal analysis, Data curation, Conceptualization.

Declaration of competing interest

The authors declare the following financial interests/personal relationships which may be considered as potential competing interests: Federico Montoncello reports financial support was provided by Dipartimento di Fisica e Scienze della Terra, Università degli Studi di Ferrara. Ezio Iacocca reports financial support was provided by National Science Foundation. Alison Roxburgh reports financial support was provided by National Science Foundation. Pietro Micaletti reports financial support was provided by Dipartimento di Fisica e Scienze della Terra, Università degli Studi di Ferrara. Moreno Marzolla declares no known competing financial interests or personal relationships that could have appeared to influence the work reported in this paper.

Acknowledgments

P.M. and F.M. acknowledge support by the Department of Physics and Earth Sciences-University of Ferrara Grant Bando FIRD 2023, as well as the CINECA award under the ISCRA initiative, for the availability of high performance computing resources and support (Project SWIM-3D on Leonardo). A.R. and E.I. acknowledge support by the National Science Foundation, United States under Grant No. 2205796.

Data availability

Data will be made available on request.

References

[1] H. Rahmani, D. Shetty, M. Wagih, Y. Ghasempour, V. Palazzi, N. Carvalho, R. Correia, A. Costanzo, D. Vital, F. Alimenti, J. Kettle, D. Masotti, P. Mezzanotte, L. Roselli, J. Grosinger, Next-generation IoT devices: Sustainable eco-friendly manufacturing, energy harvesting, and wireless connectivity, IEEE J. Microw. 3 (2023) 237–255.

[2] K. Rupp, 50 years of microprocessor trend data, 2022, https://github.com/karlrupp/microprocessor-trend-data.

[3] M. Waldrop, More than Moore, Nat. 530 (2016) 144–147, http://dx.doi.org/10.1038/530144a.

[4] L. Lannelongue, H. Aronson, A. Bateman, E. Birney, T. Caplan, M. Juckes, J. McEntyre, A. Morris, G. Reilly, M. Inouye, GREENER principles for environmentally sustainable computational science, Nat. Comput. Sci. 3 (2023) 514–521, http://dx.doi.org/10.1038/s43588-023-00461-y.

[5] A. Mahmoud, F. Ciubotaru, F. Vanderveken, A. Chumak, S. Hamdioui, C. Adelmann, S. Cotofana, Introduction to spin wave computing, J. Appl. Phys. 128 (2020) 161101, http://dx.doi.org/10.1063/5.0019328.

[6] G. Csaba, Á. Papp, W. Porod, Perspectives of using spin waves for computing and signal processing, Phys. Lett. A 381 (2017) 1471, http://dx.doi.org/10.1016/j.physleta.2017.02.042.

[7] M. Kaffash, SergiLendinez, M. BenjaminJungfleisch, Nanomagnonics with artificial spin ice, Phys. Lett. A 402 (2021) 127364, http://dx.doi.org/10.1016/j.physleta.2021.127364.

[8] A. Barman, G. Gubbiotti, S. Ladak, A. Adeyeye, M. Krawczyk, J. Gräfe, C. Adelmann, S. Cotofana, A. Naeemi, V. Vasyuchka, B. Hillebrands, S. Nikitov, H. Yu, D. Grundler, A. Sadovnikov, A. Grachev, S. Sheshukova, J. Duquesne, M. Marangolo, G. Csaba, W. Porod, V. Demidov, S. Urazhdin, S. Demokritov, E. Albisetti, D. Petti, R. Bertacco, H. Schultheiss, V. Kruglyak, V. Poimanov, S. Sahoo, J. Sinha, H. Yang, M. Münzenberg, T. Moriyama, S. Mizukami, P. Landeros, R. Gallardo, G. Carlotti, J. Kim, R. Stamps, R. Camley, B. Rana, Y. Otani, W. Yu, T. Yu, G. Bauer, C. Back, G. Uhrig, O. Dobrovolskiy, B. Budinska, H. Qin, S. Dijken, A. Chumak, A. Khitun, D. Nikonov, I. Young, B. Zingsem, M. Winklhofer, The 2021 magnonics roadmap, J. Phys.: Condens. Matter. 33 (2021) 413001, http://dx.doi.org/10.1088/1361-648X/abec1a.

[9] E. Iacocca, O. Heinonen, Topologically nontrivial magnon bands in artificial square spin ices with Dzyaloshinskii-Moriya interaction, Phys. Rev. Appl. 8 (2017) 034015, https://link.aps.org/doi/10.1103/PhysRevApplied.8.034015.

[10] G. Gubbiotti, L. Xiong, F. Montoncello, A. Adeyeye, Collective spin waves in arrays of permalloy nanowires with single-side periodically modulated width, Appl. Phys. Lett. 111 (2017) 192403, http://dx.doi.org/10.1063/1.5006294.

[11] H. Qin, G. Both, S. Hämäläinen, L. Yao, S. Dijken, Low-loss YIG-based magnonic crystals with large tunable bandgaps, Nat. Commun. 9 (2018).

[12] D. Kumar, J. Kłos, M. Krawczyk, A. Barman, Magnonic band structure, complete bandgap, and collective spin wave excitation in nanoscale two-dimensional magnonic crystals, J. Appl. Phys. 115 (2014) 043917, http://dx.doi.org/10.1063/1.4862911.

[13] A. Frotanpour, J. Woods, B. Farmer, A. Kaphle, L. Long, L. Giovannini, F. Montoncello, Magnetization dynamics of a Fibonacci-distorted kagome artificial spin ice, Phys. Rev. B 102 (2020) 224435.

[14] W. Bang, J. Sturm, R. Silvani, M. Kaffash, A. Hoffmann, J. Ketterson, F. Montoncello, M. Jungfleisch, Influence of the vertex region on spin dynamics in artificial kagome spin ice, Phys. Rev. Appl. 14 (2020) 014079, https://link.aps.org/doi/10.1103/PhysRevApplied.14.014079.

[15] S. Lendinez, M. Kaffash, O. Heinonen, S. Gliga, E. Iacocca, M. Jungfleisch, Nonlinear multi-magnon scattering in artificial spin ice, Nat. Commun. 14 (2023) 3419, https://www.nature.com/articles/s41467-023-38992-7.

[16] K. Mori, T. Koguchi, T. Watanabe, Y. Yoshihara, H. Miyashita, D. Grundler, M. Inoue, K. Ishiyama, T. Goto, Orientation-dependent two-dimensional magnonic crystal modes in an ultralow-damping ferrimagnetic waveguide containing repositioned hexagonal lattices of Cu disks, Phys. Rev. Appl. 21 (2024) 014061, https://link.aps.org/doi/10.1103/PhysRevApplied.21.014061.

[17] A. Roxburgh, E. Iacocca, Nano-magnonic crystals by periodic modulation of magnetic parameters, Magnetochemistry. 10 (2024) https://www.mdpi.com/2312-7481/10/3/14.

[18] Pietro Micaletti, Federico Montoncello, Dynamic footprints of the specific artificial spin ice microstate on its spin waves, Magnetochemistry (ISSN: 2312-7481) 9 (6) (2023) http://dx.doi.org/10.3390/magnetochemistry9060158, https://www.mdpi.com/2312-7481/9/6/158.

[19] J. Levy, Magnetic Structures of 2D and 3D Nanoparticles: Properties and Applications, Jenny Stanford Publishing, 2016.

[20] G. Gubbiotti, Three-Dimensional Magnonics: Layered, Micro- and Nanostructures, Jenny Stanford Publishing, Singapore, 2019.

[21] S. Sahoo, A. May, A.Den. Berg, A. Mondal, S. Ladak, A. Barman, Observation of coherent spin waves in a three-dimensional artificial spin ice structure, Nano Lett. 21 (2021) 4629, http://dx.doi.org/10.1021/acs.nanolett.1c00650.

[22] S. Ladak, A. Fernández-Pacheco, P. Fischer, Science and technology of 3D magnetic nanostructures, APL Mater. 10 (2022) 5, http://dx.doi.org/10.1063/5.0136801.

[23] J. Gartside, K. Stenning, A. Vanstone, H. Holder, D. Arroo, T. Dion, F. Caravelli, H. Kurebayashi, W. Branford, Reconfigurable training and reservoir computing in an artificial spin-vortex ice via spin-wave fingerprinting, Nat. Nanotechnol. 17 (2022) 460–469, http://dx.doi.org/10.1038/s41565-022-01091-7.

[24] J. Gartside, A. Vanstone, T. Dion, K. Stenning, D. Arroo, H. Kurebayashi, W. Branford, Reconfigurable magnonic mode-hybridisation and spectral control in a bicomponent artificial spin ice, Nat. Commun. 12 (2021) 2488, http://dx.doi.org/10.1038/s41467-021-22723-x.

[25] E. Iacocca, S. Gliga, O. Heinonen, Tailoring spin-wave channels in a reconfigurable artificial spin ice, Phys. Rev. Appl. 13 (2020) 044047, https://link.aps.org/doi/10.1103/PhysRevApplied.13.044047.

[26] T. Dion, K. Stenning, A. Vanstone, H. Holder, R. Sultana, G. Alatteili, V. Martinez, M. Kaffash, T. Kimura, R. Oulton, W. Branford, H. Kurebayashi, E. Iacocca, M. Jungfleisch, J. Gartside, Ultrastrong magnon-magnon coupling and chiral spin-texture control in a dipolar 3D multilayered artificial spin-vortex ice, Nat. Commun. 15 (2024) 4077, http://dx.doi.org/10.1038/s41467-024-48080-z.

[27] R. Negrello, F. Montoncello, M. Kaffash, M. Jungfleisch, G. Gubbiotti, Dynamic coupling and spin-wave dispersions in a magnetic hybrid system made of an artificial spin-ice structure and an extended NiFe underlayer, APL Mater. 10 (2022) 091115, http://dx.doi.org/10.1063/5.0102571.

[28] F. Montoncello, M. Kaffash, H. Carfagno, M. Doty, G. Gubbiotti, M. Jungfleisch, A brillouin light scattering study of the spin-wave magnetic field dependence in a magnetic hybrid system made of an artificial spin-ice structure and a film underlayer, J. Appl. Phys. 133 (2023) 083901, http://dx.doi.org/10.1063/5.0140866.

[29] D. Girardi, S. Finizio, C. Donnelly, G. Rubini, S. Mayr, V. Levati, S. Cuccurullo, F. Maspero, J. Raabe, D. Petti, E. Albisetti, Three-dimensional spin-wave dynamics, localization and interference in a synthetic antiferromagnet, Nat. Commun. 15 (2024) 3057, http://dx.doi.org/10.1038/s41467-024-47339-9.

[30] Y. Park, D. Kim, J. Kim, Y. Nam, M. Park, H. Choi, B. Min, S. Choe, Experimental observation of the correlation between the interfacial Dzyaloshinskii–Moriya interaction and work function in metallic magnetic trilayers, NPG Asia Mater. 10 (2018) 995–1001, http://dx.doi.org/10.1038/s41427-018-0090-x.

[31] A. Sud, S. Tacchi, D. Sagkovits, C. Barton, M. Sall, L. Diez, E. Stylianidis, N. Smith, L. Wright, S. Zhang, X. Zhang, D. Ravelosona, G. Carlotti, H. Kurebayashi, O. Kazakova, M. Cubukcu, Tailoring interfacial effect in multilayers with Dzyaloshinskii–Moriya interaction by helium ion irradiation, Sci. Rep. 11 (2021) 23626, http://dx.doi.org/10.1038/s41598-021-02902-y.

[32] Z. Wang, H. Yuan, Y. Cao, Z. Li, R. Duine, P. Yan, Magnonic frequency comb through nonlinear Magnon-Skyrmion scattering, Phys. Rev. Lett. 127 (2021) 037202, https://link.aps.org/doi/10.1103/PhysRevLett.127.037202.

[33] J. Flores-Farìas, D. Cortés-Ortuño, F. Brevis, P. Landeros, R. Gallardo, Selective nonreciprocal localization of flat magnonic modes induced by a periodic Dzyaloshinskii-Moriya interaction, Phys. Rev. B 109 (2024) 054423, https://link.aps.org/doi/10.1103/PhysRevB.109.054423.

[34] N. Gusev, A. Sadovnikov, S. Nikitov, M. Sapozhnikov, O. Udalov, Manipulation of the Dzyaloshinskii–Moriya interaction in Co/Pt multilayers with strain, Phys. Rev. Lett. 124 (2020) 157202, https://link.aps.org/doi/10.1103/PhysRevLett.124.157202.

[35] J. Kharlan, K. Szulc, J. Kłos, G. Centała, Tunable magnonic crystal in a hybrid superconductor–ferrimagnet nanostructure, 2024, https://arxiv.org/abs/2408.01240.

[36] I. Golovchanskiy, N. Abramov, V. Stolyarov, P. Dzhumaev, O. Emelyanova, A. Golubov, V. Ryazanov, A. Ustinov, Ferromagnet/superconductor hybrid magnonic metamaterials, Adv. Sci. 6 (2019) 1900435, https://onlinelibrary.wiley.com/doi/abs/10.1002/advs.201900435.

[37] I. Golovchanskiy, N. Abramov, V. Stolyarov, V. Chichkov, M. Silaev, I. Shchetinin, A. Golubov, V. Ryazanov, A. Ustinov, M. Kupriyanov, Magnetization dynamics in proximity-coupled superconductor-ferromagnet-superconductor multilayers, Phys. Rev. Appl. 14 (2020) 024086, https://link.aps.org/doi/10.1103/PhysRevApplied.14.024086.

[38] I. Golovchanskiy, N. Abramov, V. Stolyarov, A. Golubov, V. Ryazanov, A. Ustinov, Nonlinear spin waves in ferromagnetic/superconductor hybrids, J. Appl. Phys. 127 (2020) 093903, http://dx.doi.org/10.1063/1.5141793.

[39] K. Szulc, M. Zelent, M. Krawczyk, Reconfigurable spin-wave platform based on interplay between nanodots and waveguide in hybrid magnonic crystal, 2024.

[40] Even though outside the field of 3D-Magnonics, interestingly in Ref. [89] a sinusoidal field was implemented by electric current flowing through a meander-type geometry.

[41] A. Chumak, P. Kabos, M. Wu, C. Abert, C. Adelmann, A. Adeyeye, J. Åkerman, F. Aliev, A. Anane, A. Awad, C. Back, A. Barman, G. Bauer, M. Becherer, E. Beginin, V. Bittencourt, Y. Blanter, P. Bortolotti, I. Boventer, D. Bozhko, S. Bunyaev, J. Carmiggelt, R. Cheenikundil, F. Ciubotaru, S. Cotofana, G. Csaba, O. Dobrovolskiy, C. Dubs, M. Elyasi, K. Fripp, H. Fulara, I. Golovchanskiy,

C. Gonzalez-Ballestero, P. Graczyk, D. Grundler, P. Gruszecki, G. Gubbiotti, K. Guslienko, A. Haldar, S. Hamdioui, R. Hertel, B. Hillebrands, T. Hioki, A. Houshang, C. Hu, H. Huebl, M. Huth, E. Iacocca, M. Jungfleisch, G. Kakazei, A. Khitun, R. Khymyn, T. Kikkawa, M. Kläui, O. Klein, J.Kł. os, S. Knauer, S. Koraltan, M. Kostylev, M. Krawczyk, I. Krivorotov, V. Kruglyak, D. Lachance-Quirion, S. Ladak, R. Lebrun, Y. Li, M. Lindner, R. Macêdo, S. Mayr, G. Melkov, S. Mieszczak, Y. Nakamura, H. Nembach, A. Nikitin, S. Nikitov, V. Novosad, J. Otálora, Y. Otani, A. Papp, B. Pigeau, P. Pirro, W. Porod, F. Porrati, H. Qin, B. Rana, T. Reimann, F. Riente, O. Romero-Isart, A. Ross, A. Sadovnikov, A. Safin, E. Saitoh, G. Schmidt, H. Schultheiss, K. Schultheiss, A. Serga, S. Sharma, J. Shaw, D. Suess, O. Surzhenko, K. Szulc, T. Taniguchi, M. Urbánek, K. Usami, A. Ustinov, T. Sar, S. Dijken, V. Vasyuchka, R. Verba, S. Kusminskiy, Q. Wang, M. Weides, M. Weiler, S. Wintz, S. Wolski, X. Zhang, Advances in magnetics roadmap on spin-wave computing, IEEE Trans. Magn. 58 (2022) 1–72.

[42] H. Fuller, M. Hale, Determination of magnetization distribution in thin films using electron microscopy, J. Appl. Phys. 31 (1960) 238–248, http://dx.doi.org/10.1063/1.1735552.

[43] K. Harte, Theory of magnetization ripple in ferromagnetic films, J. Appl. Phys. 39 (1968) 1503–1524, http://dx.doi.org/10.1063/1.1656388.

[44] H. Hoffmann, Theory of magnetization ripple, IEEE Trans. Magn. 4 (1968) 32–38.

[45] H. Riedel, Micromagnetic theory of large-angle ripples and stripe domains in thin ferromagnetic films, Phys. Status Solidi (a). 24 (1974) 449–460, https://onlinelibrary.wiley.com/doi/abs/10.1002/pssa.2210240209.

[46] 3D Magnonics is a relatively recent research field where the magnon excitation and propagation properties are studied and designed as emerging from the interactions occurring along all the three Cartesian directions. As a consequence, magnon control at the nanoscale is attained by the design of the geometric and magnetic structure along the three directions. It must be considered distinct from the concept of 3D magnonic crystal (a ferromagnetic diffraction grating where periodicity is along all the three directions), which is rather a subset field of 3D Magnonics. In particular, 3D stacks of layers are considered a subject of 3D Magnonics, even when periodicity (and magnon propagation) is along two or even one direction only, as in our case [20].

[47] A. Fernández-Pacheco, R. Streubel, O. Fruchart, R. Hertel, P. Fischer, R. Cowburn, Three-dimensional nanomagnetism, Nat. Commun. 8 (2017) 15756, http://dx.doi.org/10.1038/ncomms15756.

[48] A. Vansteenkiste, J. Leliaert, M. Dvornik, M. Helsen, F. Garcia-Sanchez, B. Van Waeyenberge, The design and verification of MuMax3, AIP Adv. 4 (2014) 107133.

[49] Hans Fangohr, Giuliano Bordignon, Matteo Franchin, Andreas Knittel, Peter A. J. de Groot, Thomas Fischbacher, A new approach to (quasi) periodic boundary conditions in micromagnetics: The macrogeometry, J. Appl. Phys. (ISSN: 0021-8979) 105 (7) (2009) 07D529, http://dx.doi.org/10.1063/1.3068637, arXiv:https://pubs.aip.org/aip/jap/article-pdf/doi/10.1063/1.3068637/15589855/07d529_1_online.pdf.

[50] R. Damon, J. Eshbach, Magnetostatic modes of a ferromagnet slab, J. Phys. Chem. Solids 19 (1961) 308–320, https://www.sciencedirect.com/science/article/pii/0022369761900415.

[51] H. Braun, Topological effects in nanomagnetism: from superparamagnetism to chiral quantum solitons, Adv. Phys. 61 (2012) 1–116, http://dx.doi.org/10.1080/00018732.2012.663070.

[52] F. Brevis, L. Körber, R. Gallardo, A. Kákay, P. Landeros, The toroidal moments in confined nanomagnets and its impact on magnonics, 2024, https://arxiv.org/abs/2412.13309.

[53] B. Wiele, F. Montoncello, A continuous excitation approach to determine time-dependent dispersion diagrams in 2D magnonic crystals, J. Phys. D: Appl. Phys. 47 (2014) 315002, http://dx.doi.org/10.1088/0022-3727/47/31/315002.

[54] G. Venkat, D. Kumar, M. Franchin, O. Dmytriiev, M. Mruczkiewicz, H. Fangohr, A. Barman, M. Krawczyk, A. Prabhakar, Proposal for a standard micromagnetic problem: spin wave dispersion in a magnonic waveguide, IEEE Trans. Magn. 49 (2013) 524, https://ieeexplore.ieee.org/document/6228538.

[55] C. Kittel, P. McEuen, Introduction to Solid State Physics, John Wiley and Sons, 2015.

[56] R. McMichael, B. Maranville, Edge saturation fields and dynamic edge modes in ideal and nonideal magnetic film edges, Phys. Rev. B 74 (2006) 024424, https://link.aps.org/doi/10.1103/PhysRevB.74.024424.

[57] J. Shaw, T. Silva, M. Schneider, R. McMichael, Spin dynamics and mode structure in nanomagnet arrays: Effects of size and thickness on linewidth and damping, Phys. Rev. B 79 (2009) 184404, https://link.aps.org/doi/10.1103/PhysRevB.79.184404.

[58] G. Gubbiotti, G. Carlotti, T. Okuno, M. Grimsditch, L. Giovannini, F. Montoncello, F. Nizzoli, Spin dynamics in thin nanometric elliptical permalloy dots: A Brillouin light scattering investigation as a function of dot eccentricity, Phys. Rev. B 72 (2005) 184419, https://link.aps.org/doi/10.1103/PhysRevB.72.184419.

[59] R. Zivieri, F. Montoncello, L. Giovannini, F. Nizzoli, S. Tacchi, M. Madami, G. Gubbiotti, G. Carlotti, A. Adeyeye, Collective spin modes in chains of dipolarly interacting rectangular magnetic dots, Phys. Rev. B 83 (2011) 054431, https://link.aps.org/doi/10.1103/PhysRevB.83.054431.

[60] F. Montoncello, G. Gubbiotti, Controlling the three dimensional propagation of spin waves in continuous ferromagnetic films with an increasing out of plane undulation, Sci. Rep. 11 (2021) 21344, http://dx.doi.org/10.1038/s41598-021-00479-0.

[61] M. Tinkham, Group Theory and Quantum Mechanics, Dover Publications, 2003.

[62] S. Mamica, M. Krawczyk, M. Sokolovskyy, J. Romero-Vivas, Large magnonic band gaps and spectra evolution in three-dimensional magnonic crystals based on magnetoferritin nanoparticles, Phys. Rev. B 86 (2012) 144402, https://link.aps.org/doi/10.1103/PhysRevB.86.144402.

[63] K. Böer, U. Pohl, The origin of band structure, Semicond. Phys. (2017) 1–20, http://dx.doi.org/10.1007/978-3-319-06540-3.

[64] H. Sun, D. Bhowmick, B. Yang, P. Sengupta, Interacting topological Dirac magnons, Phys. Rev. B 107 (2023) 134426, https://link.aps.org/doi/10.1103/PhysRevB.107.134426.

[65] L. Giovannini, Dirac magnons in honeycomb nanostructures, Phys. Rev. B 107 (2023) 104418, https://link.aps.org/doi/10.1103/PhysRevB.107.104418.

[66] S. Pershoguba, S. Banerjee, J. Lashley, J. Park, H. AAgren, G. Aeppli, A. Balatsky, Dirac magnons in honeycomb ferromagnets, Phys. Rev. X 8 (2018) 011010, https://link.aps.org/doi/10.1103/PhysRevX.8.011010.

[67] S. Mamica, M. Krawczyk, Reversible tuning of omnidirectional band gaps in two-dimensional magnonic crystals by magnetic field and in-plane squeezing, Phys. Rev. B 100 (2019) 214410, https://link.aps.org/doi/10.1103/PhysRevB.100.214410.

[68] R. Gallardo, P. Alvarado-Seguel, T. Schneider, C. Gonzalez-Fuentes, A. Roldán-Molina, K. Lenz, J. Lindner, P. Landeros, Spin-wave non-reciprocity in magnetization-graded ferromagnetic films, New J. Phys. 21 (2019) 033026, http://dx.doi.org/10.1088/1367-2630/ab0449.

[69] C. Herring, C. Kittel, On the theory of spin waves in ferromagnetic media, Phys. Rev. 81 (1951) 869–880, https://link.aps.org/doi/10.1103/PhysRev.81.869.

[70] B. Kalinikos, A. Slavin, Theory of dipole-exchange spin wave spectrum for ferromagnetic films with mixed exchange boundary conditions, J. Phys. C: Solid State Phys. 19 (1986) 7013, http://dx.doi.org/10.1088/0022-3719/19/35/014.

[71] S. Mamica, The influence of the demagnetizing field on the concentration of spin wave energy in two-dimensional magnonic crystals, J. Magn. Magn. Mater. 588 (2023) 171395, https://www.sciencedirect.com/science/article/pii/S0304885323010454.

[72] C. Kittel, On the theory of ferromagnetic resonance absorption, Phys. Rev. 73 (1948) 155.

[73] M. Bailleul, R. Höllinger, C. Fermon, Microwave spectrum of square permalloy dots: Quasisaturated state, Phys. Rev. B 73 (2006) 104424, https://link.aps.org/doi/10.1103/PhysRevB.73.104424.

[74] J. Jorzick, S. Demokritov, B. Hillebrands, M. Bailleul, C. Fermon, K. Guslienko, A. Slavin, D. Berkov, N. Gorn, Spin wave wells in nonellipsoidal micrometer size magnetic elements, Phys. Rev. Lett. 88 (2002) 047204, https://link.aps.org/doi/10.1103/PhysRevLett.88.047204.

[75] J. Park, P. Eames, D. Engebretson, J. Berezovsky, P. Crowell, Spatially resolved dynamics of localized spin-wave modes in ferromagnetic wires, Phys. Rev. Lett. 89 (2002) 277201, https://link.aps.org/doi/10.1103/PhysRevLett.89.277201.

[76] K. Guslienko, R. Chantrell, A. Slavin, Dipolar localization of quantized spin-wave modes in thin rectangular magnetic elements, Phys. Rev. B 68 (2003) 024422, https://link.aps.org/doi/10.1103/PhysRevB.68.024422.

[77] G. Gubbiotti, L. Xiong, F. Montoncello, L. Giovannini, A. Adeyeye, Spin wave dispersion and intensity correlation in width-modulated nanowire arrays: A Brillouin light scattering study, J. Appl. Phys. 124 (2018) 083903, http://dx.doi.org/10.1063/1.5047393.

[78] D. Kuźma, F. Montoncello, P. Sobieszczyk, A. Wal, L. Giovannini, P. Zieliński, Spin wave propagation properties across configurational antiferro/ferro-magnetic transitions, J. Appl. Phys. 124 (2018) 223902, http://dx.doi.org/10.1063/1.5057419.

[79] V. Kruglyak, M. Dvornik, R. Mikhaylovskiy, O. Dmytriiev, G. Gubbiotti, S. Tacchi, M. Madami, G. Carlotti, F. Montoncello, L. Giovannini, R. Zivieri, J. Klos, M. Sokolovskyy, S. Mamica, M. Krawczyk, M. Okuda, J. Eloi, S. Jones, W. Schwarzacher, T. Schwarze, F. Brandl, D. Grundler, D. Berkov, E. Semenova, N. Gorn, Magnonic metamaterials, Metamaterial (2012) http://dx.doi.org/10.5772/37454.

[80] O. Haas, B. Dufay, S. Saez, Development of a magnonic-based magnetic sensor: Comparison of two different implementations with YIG material, IEEE Trans. Magn. 59 (2023) 1–6.

[81] M. Sarker, H. Yamahara, L. Yao, S. Tang, Z. Liao, M. Seki, H. Tabata, Sensitivity enhancement in magnetic sensor using CoFeB/Y3Fe5O12 resonator, Sci. Rep. 12 (2022) 11105, http://dx.doi.org/10.1038/s41598-022-15317-0.

[82] C. Degen, F. Reinhard, P. Cappellaro, Quantum sensing, Rev. Modern Phys. 89 (2017) 035002, https://link.aps.org/doi/10.1103/RevModPhys.89.035002.

[83] S. Demokritov, A. Slavin, Spin waves, in: Handbook of Magnetism and Magnetic Materials, 2021, pp. 281–346, http://dx.doi.org/10.1007/978-3-030-63210-6.

[84] C. Duan, J. Velev, R. Sabirianov, Z. Zhu, J. Chu, S. Jaswal, E. Tsymbal, Surface magnetoelectric effect in ferromagnetic metal films, Phys. Rev. Lett. 101 (2008) 137201, https://link.aps.org/doi/10.1103/PhysRevLett.101.137201.

[85] M. Staruch, D. Gopman, Y. Iunin, R. Shull, S. Cheng, K. Bussmann, P. Finkel, Reversible strain control of magnetic anisotropy in magnetoelectric heterostructures at room temperature, Sci. Rep. 6 (2016) 37429, http://dx.doi.org/10.1038/srep37429.

[86] S. Hämäläinen, F. Brandl, K. Franke, D. Grundler, S. Dijken, Tunable short-wavelength spin-wave emission and confinement in anisotropy-modulated multiferroic heterostructures, Phys. Rev. Appl. 8 (2017) 014020, https://link.aps.org/doi/10.1103/PhysRevApplied.8.014020.

[87] T. Lahtinen, J. Tuomi, S. Dijken, Pattern transfer and electric-field-induced magnetic domain formation in multiferroic heterostructures, Adv. Mater. 23 (2011) 3187–3191, https://onlinelibrary.wiley.com/doi/abs/10.1002/adma.201100426.

[88] T. Lahtinen, K. Franke, S. Dijken, Electric-field control of magnetic domain wall motion and local magnetization reversal, Sci. Rep. 2 (2012) 258, http://dx.doi.org/10.1038/srep00258.

[89] A V Chumak, T Neumann, A A Serga, B Hillebrands, M P Kostylev, A current-controlled, dynamic magnonic crystal, J. Phys. D: Appl. Phys. 42 (20) (2009) 205005, http://dx.doi.org/10.1088/0022-3727/42/20/205005.